



ELSEVIER

Surface and Coatings Technology 162 (2002) 79–92

**SURFACE
& COATINGS
TECHNOLOGY**

www.elsevier.com/locate/surfcoat

Optical measurements of plasma velocity and temperature in a low-rate, low-power LPPS system

H. Hamatani^{1,*}, W.S. Crawford, M.A. Cappelli

Department of Mechanical Engineering, High Temperature Gasdynamics Laboratory, Stanford University, Stanford, CA, 94305-3032, USA

Received 17 May 2002; accepted in revised form 16 August 2002

Abstract

Low-pressure plasma spraying (LPPS) is a promising method of applying coatings to surfaces for thermal, chemical, and mechanical protection. The deposition of coatings with superior properties requires an improved understanding of this complex spray process, including the detailed understanding of the time–temperature and chemical history to which an injected particle is exposed during its travel through the high-temperature and high-velocity plasma jet. In this paper, we report on measurements of the temperatures and velocities within the plasma in a low-pressure argon–hydrogen arcjet spray plasma being developed for mesoscale manufacturing of mechanical components. The measurements reported here make use of laser absorption, laser-induced fluorescence, and optical emission spectroscopy of the H α Balmer transition in atomic hydrogen. Both the absorption and fluorescence methods take advantage of the well-known spectral line broadening of atomic hydrogen, to extract the arcjet temperature and electron density. Jet axial velocities are measured via the time of flight, as detected by optical emission, of convected disturbances caused by intrinsic fluctuations in the arc voltage. Measurements made for various anode (nozzle) geometries indicate that relatively low ($\sim 1 \text{ km s}^{-1} \text{ mm}^{-1}$) velocity gradients in the axial direction could be achieved with nozzles that include an expanding section of 10° half-angles. The measured temperatures and velocities suggest the presence of complex gas-dynamic shock structures in the arcjet plume, depending on the particular nozzle length and expansion section.

© 2002 Elsevier Science B.V. All rights reserved.

Keywords: Low pressure plasma spraying; Laser absorption; Laser-induced fluorescence; Arcjet temperature; Electron density; Jet axial velocity

1. Introduction

Conventional thermal spray processes operate at relatively high power (30–120 kW), have relatively high deposition rates (50–100 g min⁻¹) and are capable of depositing most materials that have a liquid phase [1]. Among many advanced spray-coating technologies that are used to deposit thick (thickness greater than 1 mm) chemical and thermal protective barriers, plasma spraying is considered to be one of the most effective and most widely used. However, conventional plasma sprayed coatings, along with other spray coating methods, often have a relatively low strength compared to

bulk materials. This problem, or the related problem of low adhesion strength to the substrate, may preclude the use of these coatings in applications requiring uniformly high mechanical strength.

The strength of sprayed coatings depends substantially on features, such as porosity and interlamellar strength, that exist because the coatings are built of solidified droplets, or splats. These features result from the splat process on the substrate, and thus the properties of coatings have been correlated closely to the temperature and velocity of particles upon impact [2]. The incomplete melting of injected particles is often the primary reason for a low spraying efficiency and a low bulk strength and adhesion strength. Particles' temperatures and velocities typically sustain higher values in low-pressure plasma spraying (LPPS) than in atmospheric-pressure plasma spraying (APS) [1]. LPPS processing can accommodate a wide range of materials, including

*Corresponding author. Fax: +81-43-80-2745.

E-mail address: hamatani@re.nsc.co.jp (H. Hamatani).

¹ On leave from the Nippon Steel Corporation, Welding & Joining Laboratory, 20-1 Shintomi, Futtsu, Chiba, 293-8511, Japan.

refractory metals and ceramics, with its high capacity for melting and fusing particles.

The exclusion of air from the vacuum chamber also prevents oxidation of the particle or substrate at elevated temperature. Higher limits on substrate temperature allow two advantages: increased adhesion strength by diffusion at the substrate/coating interface; and, greater control over post-process residual stress, which is directly related to the temperature gradient in the system during processing.

Due to several factors, LPPS coatings thus often demonstrate higher adhesion strength, higher bulk strength, and lower porosity, especially in metallic systems, than do APS coatings. Studies have shown LPPS to improve the overall properties of sprayed metallurgical coatings [3].

The (velocity, temperature) state of sprayed particles is also important for determining the true microstructure of coatings, including cases such as deposition of alloy or compound feedstock [4], or spraying in reactive gases [5]. For alloys or compounds, the cooling rate is critical for determining grain size and phases present, and the state of the impacting particle helps to determine the cooling rate [6]. For reactive spraying, the state of the particle helps to determine the extent of reaction in flight. Of course, the thermodynamic state of the reactive gas is similarly important.

In fact, the conditions of the plasma gas are critical in all spray cases. Due to heat and momentum transfer, the state of particles depends critically on the temperature and velocity fields of the plasma jet itself. These interactions have been modeled fairly extensively [7]. Knowledge of the plasma temperature and velocity fields is important during the design stage of a plasma spray process, when model predictions and well-designed experiments can help to guide the choice of many other key process parameters [7].

The current study is motivated by the development of low-power LPPS technology suitable for the rapid prototyping of mesoscale mechanical devices using shape-deposition manufacturing methods [8]. These mechanical systems, such as micro gas turbine engines [9], require materials to have properties comparable to the bulk cast properties, and, in some cases, must be deposited in a layer-by-layer fashion in order to achieve complex three-dimensional shapes.

This paper describes the measurement of plasma temperatures and plasma velocities in an arcjet plume. This plasma jet is a low-power LPPS source that we have developed and used recently to spray thick copper coatings of relatively high bulk mechanical strength at very low deposition rates (approx. 0.1 g min^{-1}) and low arc powers (2–4 kW) [10]. As shown here, the jet properties are strongly dependent on the geometry of the anode (nozzle) and on the overall operating conditions. Knowledge of this dependence has guided our

selection of spray conditions and configurations needed to extend this process to more challenging structural materials such as stainless steel and alloys of titanium and aluminum, and possibly to reactively sprayed metal-nitrides.

The plasma gas used here was a mixture of hydrogen and argon. Argon–hydrogen mixtures are widely used in LPPS. Hydrogen is added to argon to increase the overall plasma enthalpy at a fixed discharge current (higher operating voltage), and to increase the plasma thermal conductivity. These two effects enhance the heating of particles. The presence of electronically excited atomic hydrogen in the jet also provides a convenient spectroscopic means of probing temperature and velocity, since it is a strong radiator at 438 nm and 656 nm, the wavelengths corresponding to the Balmer- β and Balmer- α electronic transitions, respectively. Our laboratory has used optical emission, laser absorption, and laser-induced fluorescence (LIF) extensively in the past [11], to understand the properties of arc-heated hydrogen flows. The 656 nm transition is readily accessed by modern tunable narrow-band laser sources to permit interrogation of this transition with high spectral resolution. The following discussion regards spectroscopic measurements of this Balmer- α transition in the H atoms present in the LPPS jet.

2. Measurement and analysis techniques implemented

2.1. Lineshape analysis

2.1.1. Relevant broadening mechanisms

When the signal intensity of absorption or LIF is plotted vs. wavelength or wavenumber, the shape of a peak (or *lineshape*) carries information on temperature and velocity distribution of the optically active particles. The peak is broadened by various mechanisms that create a distribution in the energies of photons absorbed or emitted, in the absorption or LIF case, respectively.

Doppler broadening of the spectral peak is due to the distribution of velocities of the absorbing or fluorescing H atoms. Thus, the degree of Doppler broadening can be used to measure the translational temperature of these atoms. At typical pressures for LPPS, thermal equilibrium exists between H atoms and the other atomic and molecular species present. Doppler broadening alone produces a Gaussian profile.

Stark broadening is caused by interactions of electronically excited atoms with the microfields around charged particles, namely ions and free electrons, in the plasma [12]. Analysis of the degree of Stark broadening can yield the density of ions and electrons (*plasma*

density), for sufficiently high plasma densities [13]. Stark broadening alone produces a Lorentzian profile.

Under plasma conditions that produce amounts of both Doppler and Stark broadening that are discernible and comparable in magnitude, both effects can be measured on a single peak. The profile that is generated by the convolution of a Gaussian profile and a Lorentzian profile, provided that the two broadening mechanisms are statistically independent, is known as a Voigt profile.

For the plasma densities expected near the exit of the arcjet ($n_e > 3 \times 10^{19} \text{ m}^{-3}$), Stark broadening due to interactions between the excited hydrogen atoms and the background ions or electrons cannot be neglected [14,15]. Thus, H-atom translational temperature and electron density were determined as the two parameters in a Voigt fit to the measured Balmer- α spectral lineshape taken by absorption or LIF. Both broadening mechanisms contribute to the measured width of the spectral line. They are distinguishable since they affect the shape of the line in different ways.

In fitting the data, the Voigt-shaped five partially resolvable fine structure components are summed to obtain the overall lineshape, $\phi_V(\nu)$:

$$\phi_V(\nu) = \sum_{i=1}^5 R_i \phi_{V_i}(\nu) \quad (1)$$

where $\phi_{V_i}(\nu)$ is the spectral lineshape for each of the five fine structure components, and R_i is the relative line strength. Letting the third line be the center, the five fine-structure peaks are located at the following positions in wavenumbers (cm^{-1}): -0.144 , -0.036 , 0 , 0.22 , 0.328 . Although the overall linewidths were greater than the spacing of the fine structure, the fine structure components affected the overall shape substantially. The resolution of the measurement was 0.005 cm^{-1} .

2.1.2. The effect of gas mixture on Stark broadening

When hydrogen ions constitute the ionic population of the plasma, the full width at half-maximum (FWHM) of the Stark broadening contribution to the Voigt lineshape is well approximated, for this intermediate regime of n_e , by the empirical relation [16]:

$$\log \Delta \lambda_S = 0.027 n_e^{0.09} - 3.3 \quad (\text{nm}, \text{m}^{-3}) \quad (2)$$

However, as described above, the plasma gases used in plasma spraying are usually mixtures. In the gas mixtures studied here, which consist of at least 55 mol% argon prior to dissociation of hydrogen, one must consider the possibility that argon ions are also important perturbers in the observed Stark broadening. Stehlé and Feautrier [17] showed the dependence on ion properties in an approximate analytical expression for the ion-induced Stark width of H_α :

$$\Delta \nu_{S,I} = 1.55 \times 10^{-4} n_I \left(\frac{m_{I-H}^*}{m_e} \right)^{0.5} \frac{1}{\sqrt{T_I}} \left\{ 27.54 + \ln \left[\frac{T_e T_I^2}{(T_e + T_I) n_I m_{I-H}^*} \right] \right\} \quad (\text{Hz}, \text{cm}^{-3}, \text{K}) \quad (3)$$

where n_I is the ion density, m_{I-H}^* is the reduced mass of the pair of ion and H-atom, and T_I , T_e , and m_e are the ion and electron temperatures and electron mass, respectively. Eq. (3) assumes the *impact limit* for the Stark effect, in which thermal motion of the ions is important. This assumption is appropriate for electron densities up to approximately 10^{20} m^{-3} [14]. For a mixture containing both H^+ and Ar^+ , assuming that the different ions have the same temperature, Eq. (3) yields approximately

$$\frac{\Delta \nu_{S,Ar^+}}{\Delta \nu_{S,H^+}} \approx \frac{n_{Ar^+}}{n_{H^+}} \left(\frac{m_{Ar^+-H}^*}{m_{H^+-H}^*} \right)^{0.5} \quad (4)$$

Eq. (4) illustrates, for the case of argon, the two ways in which the presence of other species may not have an appreciable effect on the Stark broadening of the H_α line. First, the contribution of argon ions to the linewidth is proportional to their density. Using the Saha equation (assuming local thermodynamic equilibrium) as a guideline, we expect the ratio n_{Ar^+}/n_{H^+} to be only approximately 0.01–0.1 for the upper range of jet temperatures measured, 3750–6000 K. Furthermore, due to the use of the reduced mass in Eqs. (3) and (4), the effect of perturber mass on linewidth is limited. The quantity $m_{Ar^+-H}^*/m_{H^+-H}^*$ equals 1.95, so the Stark linewidth per unit density for argon ions exceeds that for hydrogen ions by only 40%. Using these values in Eq. (4), argon ions are expected to contribute less than 14% to the overall Stark broadening, implying that the pure-hydrogen relation, Eq. (2), is a valid approximation for these argon–hydrogen mixtures at these temperatures.

It should be pointed out that peak plasma temperatures at the arc have been measured at approximately 10 000 K for a similar arcjet on pure hydrogen [18]. In Saha equilibrium at 10 000 K, Eq. (4) predicts nearly equal contributions from Ar^+ and H^+ to the Stark linewidth. Near the arc, therefore, or in the case of frozen chemistry that has been established by an arc, Eq. (2) must be replaced with an expression that accounts for the contribution of argon ions to the Stark effect.

2.2. Velocity measurements by Doppler shifted peaks (Doppler shift velocimetry)

Besides lineshape measurements, the component of bulk velocity in the direction of view can be inferred from a net Doppler shift, of the entire spectral peak,

relative to the peak observed for a stationary gas [19]. In our facility, however, the axial view was prevented by the presence of a substrate holder for spray deposition studies. This obstruction precluded the use of LIF to measure axial velocities.

2.3. Velocity measurements by fluctuation propagation

In the present study, we instead measured the axial plume velocity by timing the propagation of variations in the excited-state density induced by natural fluctuations in the arc discharge power. These normally-occurring disturbances arise from small fluctuations in the power supply voltage that compensate for instabilities in the attachment of the arc root on the anode [20]. The resulting fluctuations in the 656 nm line emission were tracked at two known axial locations and the delay between the arrivals of disturbances in emission was attributed to the finite mean velocity. To determine with accuracy the temporal shift in the two emission waveforms, a cross-correlation operation was applied to the time-dependent signals on the two detectors. Thus, the average velocity over the sampling time was measured. We shall refer to this method as the *emission correlation method* for plasma velocity measurements. Pobst et al. [21] used this method in a pure hydrogen arcjet and showed it to be consistent with measurements made using LIF.

Pobst et al. [21] also developed a similar method with finer temporal resolution, called current modulation velocimetry (CMV), in order to resolve the dependence of velocity on the phase of the fluctuation waveform itself. This resolution was not necessary for plasma spray studies, because particles are accelerated and heated slowly as compared to the frequency of fluctuations. The calculated characteristic time scales for acceleration and heating of particles in this system are on the order of 0.1–1 ms, whereas the period of fluctuation for the power supply was less than 10 μ s. Also, CMV may not be desirable when temporal resolution is not necessary, because it requires external perturbation of the arc current.

The setup used here differs slightly from that of Pobst et al. by using precision-mounted optical fibers to facilitate the precise spacing of collection sites. It also represents a hybrid of the two methods highlighted in Pobst et al. [21], using two PMTs for spatial resolution while averaging temporally. Fig. 1 shows a schematic diagram of the optical setup used here for the correlation method.

2.4. Knudsen number criteria for applying the correlation method

With filters passing only the emission near 656 nm, the only velocity measured directly by the correlation

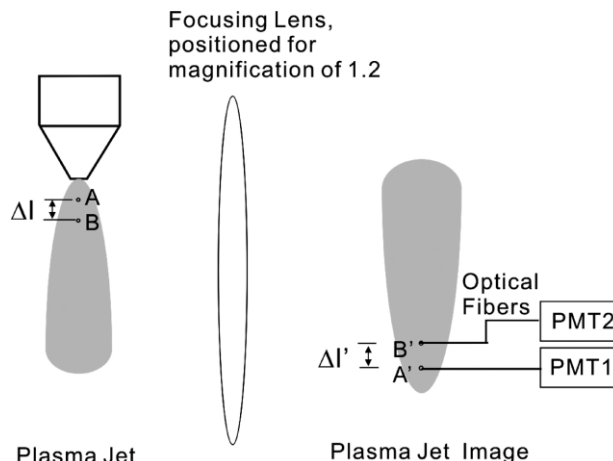


Fig. 1. Schematic diagram of the experimental setup for velocity measurements by the correlation method. Fiber separation distance $\Delta l'$ was varied in the range of 1–3 mm.

method was that of excited hydrogen atoms in the plasma. There are two criteria that should be satisfied to assert that this velocity equals that of the other plasma constituents.

Most importantly, if the flow is in the continuum regime, then the mean velocities of the various species are equal. The relevant criterion is

$$\text{Kn}_d = \frac{\lambda}{d} \ll 1 \quad (5)$$

where λ is the mean free path between particles in the mixture, and d is a characteristic length of the jet such as the jet diameter. In the studied region of this plasma jet, λ is typically in the range of 30–60 μ m for argon and 200–400 μ m for atomic hydrogen. The pressures in the jet are not known exactly, but due to its relatively small area ratio in the diverging section, the nozzle is likely to be under-expanded for low chamber pressures. Thus, λ is calculated using the chamber pressure, and the measured temperature, to obtain an upper bound on Kn_d . An upper-bound estimate for Kn_d , for chamber pressure 5.3 kPa, is 0.1 (for H atoms at the 2 mm axial position where the jet diameter is approx. 3 mm). Since this barely satisfies the criterion, it could cast into doubt the continuum flow assumption for chamber pressures lower than 5.3 kPa, at locations very near the nozzle exit. The observed existence of relatively thin shocks, however, indicates that λ is much smaller than d for the jet conditions and regions studied here, since shock wave thickness is on the order of λ [22].

The other criterion of interest, to validate this velocity measurement in a gas mixture, relates to the number of collisions that occur between the sites at which emission is detected. Since collisions between H and Ar atoms equalize their mean velocities, the equivalence of the detected and the mixture velocity are only confirmed

for a given measurement location if several such collisions occur between detection sites. This criterion can be expressed in the form of another Knudsen number:

$$\text{Kn}_{\Delta l, \text{Ar}} = \frac{\lambda_{\text{Ar-H}}}{\Delta l} \leq \sqrt{\frac{m_{\text{H}}}{m_{\text{Ar}}}} \quad (6)$$

where $\lambda_{\text{Ar-H}}$ is the mean distance traveled by an argon atom between collisions with hydrogen atoms, and Δl is the distance between detection sites as shown in Fig. 1. The inequality in Eq. (6) gives an approximate guideline of $\text{Kn}_{\Delta l, \text{Ar}}$ less than approximately 0.16, reflecting that several such collisions are required to appreciably alter the momentum of the much heavier argon atom [23]. Thus, in regions of steep velocity gradient, the two species may exhibit different velocities over length scales less than a few $\lambda_{\text{Ar-H}}$. This consideration can establish a minimum on the detector spacing for a mixed flow, especially when the tracer specie has mass much different from other species in the flow. In the present study at 5.3 kPa, the conservatively estimated values for $\text{Kn}_{\Delta l, \text{Ar}}$ were at a maximum of approximately 0.03 near the jet exit, satisfying the inequality in Eq. (6). At 1.1 kPa, however, $\text{Kn}_{\Delta l, \text{Ar}}$ may be as high as 0.2 near the jet exit, so the maximum detected velocity may be higher than the argon velocity for the lowest pressure cases reported here.

2.5. Equilibrium assumptions for temperature measurements

The absorption and LIF techniques described here use Doppler broadening of the Balmer- α line to measure the translational temperature of atomic hydrogen. To equate this measured temperature to that of argon and any molecular hydrogen in the flow, local thermodynamic equilibrium is assumed for the mixture. The measured intensity ratios between Balmer- α and Balmer- β reflect higher temperatures, from which we infer an approximate electron temperature assuming thermal equilibrium between free electrons and the excitation state of H atoms.

2.6. Abel inversion of laser absorption data

Whereas LIF measurements are spatially resolved to within the volume of intersection of the excitation laser and the collection optics, the absorption signal represents an integral of the strongly varying plasma properties along the beam path. For a plasma plume with radial symmetry, successive absorption measurements through various lateral chords of the jet can be converted to radial data through an Abel inversion. However, the plume studied here does not satisfy the condition of radial symmetry required for accurate Abel inversion. Spectroscopic data, as well as flow visualization, indicate asymmetry in this arcjet plume. Asymmetric flow

may stem from uneven electrode wear that seems to result from slight initial misalignment of the cathode and surrounding anode/nozzle. Abel inversion was carried out for a limited data set, nonetheless, for comparison to the spatially resolved LIF temperature measurements. We have employed a segment method [24] when using the Abel inversion. Most of the absorption data shown here are instead from the basic, line-of-sight signal, in order to avoid inversion error due to asymmetry. This is described further below.

3. Experimental procedures

Fig. 2 shows the experimental setup highlighting the low-pressure plasma source, and the components used for the laser absorption and the LIF measurements. The plasma source and deposition facility consists of a 30 cm diameter by 25 cm long vacuum chamber equipped with feed through for the powder injection (the powder feeder is located outside of the vacuum chamber), water for substrate cooling, and optical ports for emission and LIF diagnostics. The plasma discharge head is a modified low-power commercial Komatsu G9401 transferred-arc cutting torch, with a redesigned cathode and anode for low-power non-transferred arc plasma spraying. Although the main body of the arc source is located inside the vacuum chamber, it is interfaced to the outside of the chamber with a compression vacuum fitting, so that all connections (power, water, plasma gas) are made outside of vacuum for convenience. Regulated current is delivered to the arc source by a Komatsu 4 kW (maximum) fine plasma power supply. The vacuum chamber is pumped by two mechanical pumps with a total capacity of 2300 cfm. It is possible to maintain chamber pressures in the range from 0.7 to 101.3 kPa during plasma spraying, although the present results are for 1.3–10.7 kPa, which is a typical range over which we have performed spray studies [10].

For LIF and absorption studies, we used a tunable external-cavity diode laser (New Focus Inc. Model 6009 10 mW maximum). For LIF, a wedged and coated beam splitter (Opto-Sigma Model 038-2460) provided a precise fraction of the beam for a coarse measure of the incident intensity (Photodiode 2 in Fig. 2) and a wavelength reference (using a Burleigh wavemeter). For absorption, the reference intensity was taken to be the transmitted beam intensity with gas flow but no arc, measured immediately prior to striking and stabilizing the arc for an absorption measurement. This alternative was chosen due to etalon problems with a different beam splitter.

In both cases, the probe beam was passed through both an optical chopper (New Focus 3501, 1.5-kHz chopping rate) for phase-sensitive discrimination against plasma emission, and a double convex lens (40 mm diameter, 400 mm focal length) that produced a tight

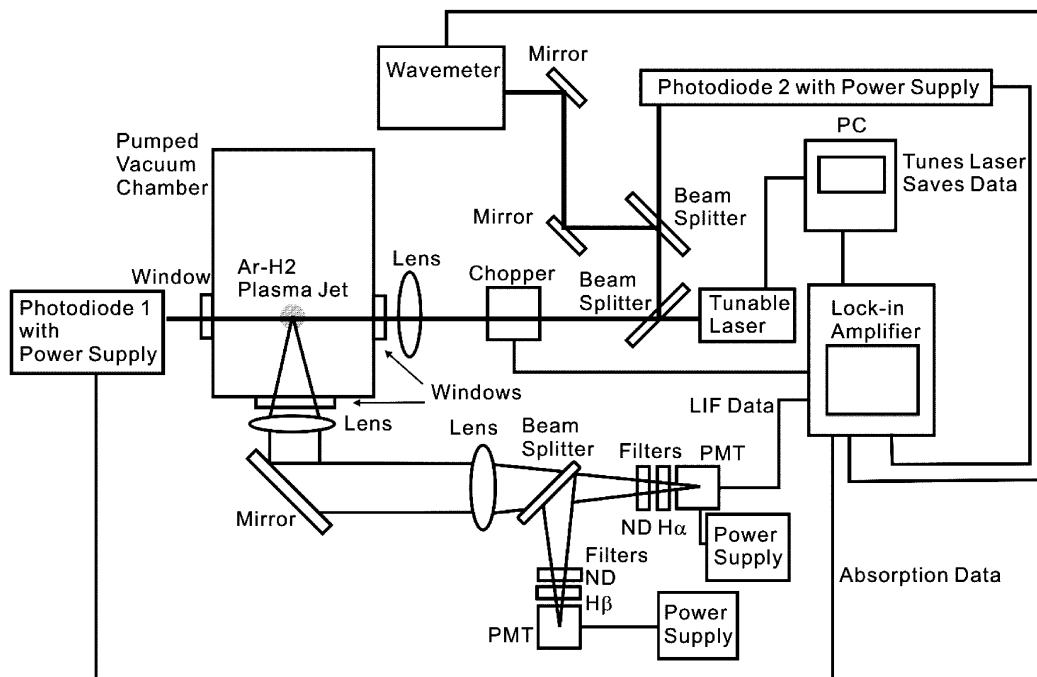


Fig. 2. Top-view schematic diagram of the experimental setup. Composite of systems for laser absorption, laser-induced fluorescence, and line-ratio measurements. Plasma jet direction is into the page.

beam waist (0.5 mm) for high spatial resolution. For absorption measurements, the intensity of the beam transmitted through the plasma was measured by a second photodiode (Photodiode 1 in Fig. 2). The transmitted laser photodiode signal was sent to a lock-in-amplifier (Stanford Research Systems SR850). A PC controlled the diode laser and the lock-in amplifier. The tuning range of the diode laser was found to be 656.39–656.56 nm. The tuning rate chosen for these studies was 0.002 nm s^{-1} . A Hamamatsu R928 photomultiplier tube (PMT) was used to detect the laser-induced fluorescence emission from the intersection of foci of the laser and the collection optics. The collection train consisted of a lens of diameter 40 mm and focal length 400 mm, neutral density filter (#2), and an interference-type bandpass filter. The bandpass filter, centered at 656.3 nm with FWHM of 11.5 nm, was used to isolate the Balmer- α emission from broadband light sources.

For some plasma conditions, this optical train was used to collect emission simultaneously from the Balmer- β transition as well, by inserting a beam splitter and second PMT instrumented with a bandpass filter centered at 438 nm. Both photomultipliers were calibrated for relative spectral response, and the ratio of the spectral line intensities for *spontaneous* emission was used to estimate the electron temperature [13].

LIF measurements are point-specific and thus offer excellent spatial resolution. Also, the LIF lineshape measurement does not require compensation for laser attenuation if the absorptance along the laser path is

wavelength-independent over the tuning range. This assumption was considered to be valid, for the room air, quartz lens and window due to the narrowness of the tuning range, and for the chamber bath gas due to its low temperature and thus negligible concentration of atomic hydrogen. A small error may have been incurred by neglecting the spectral variation of absorptance of the portion of the plasma jet through which the laser passes prior to reaching the measurement volume. However, this effect was minimized by minimizing the laser's path length through the plume.

On the other hand, the intense background plasma emission necessitated scans of relatively long duration. Integration times greater than 1 s, on the lock-in amplifier, were required in order to achieve a desired signal-to-background ratio greater than 10 at maximum fluorescence. Laser absorption measurements, conversely, do not suffer due to background emission, but they lack spatial resolution as described in the previous section.

As discussed above, axial velocities were measured by the correlation method diagrammed in Fig. 1. Plasma-induced optical emission was imaged with a bi-convex lens ($f=400 \text{ mm}$) at a magnification of $M=1.2$ onto the entrance aperture of two optical fibers (core size is $62.5 \mu\text{m}$, manufactured by Wave Optics Inc). The fibers delivered the signals to the pair of photomultipliers (Hamamatsu R928), PMT_1 and PMT_2 , respectively. The light emitted from points A and B in the plasma jet, separated by a distance Δl , was projected onto the

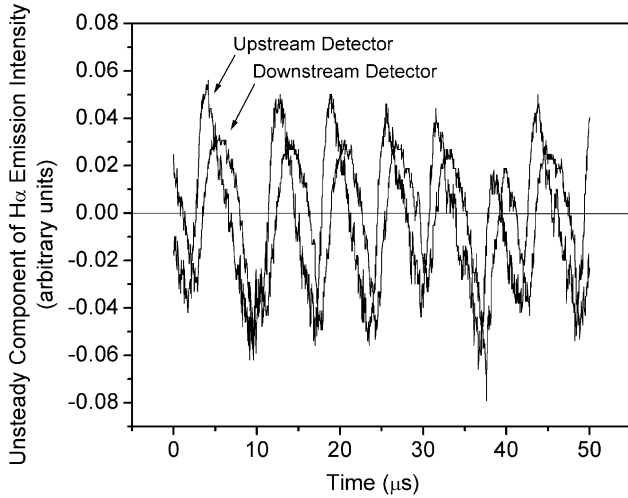


Fig. 3. Example of PMT signals for the correlation method using H_{α} emission.

locations A' and B' in the image plane, the separation of which is given by $\Delta l' = M\Delta l$. Emission from A is detected by PMT1, and that from B is detected by PMT2. Narrow bandpass interference filters were used in front of the entrance aperture to the photomultiplier detectors to isolate the spectral emission associated with the H_{α} electronic transition. When necessary, neutral density filters attenuated the signal to a level within the detectors' range for linear response. The axial distance between the fibers was varied in the range $\Delta l' = 1-3$ mm ($\pm 5 \mu\text{m}$).

The output currents from the two detectors were simultaneously measured as voltages across termination impedance on a digital storage oscilloscope. In all cases, the two signals' AC components were similar in shape, but shifted in time due to the finite convection velocity of the fluctuations in plasma emittance. As described

above, this velocity was taken to be the mean axial velocity of the emitting atoms. Fig. 3 shows a typical example of the two synchronized signals, clearly demonstrating the temporal shift. We checked the possibility of an additional phase shift due to data acquisition electronics by exchanging the two optical fibers at their output, and this had no effect on the measured time-shift.

Jet cooling and expansion reduced the density of electronically excited H atoms, and hence reduced the signal strength, as distance from the nozzle was increased.

To determine the temporal shift as an average over the sample interval $[t_1, t_2]$, between the two signals, a cross-correlation analysis of the time traces was performed, using the cross-correlation function

$$C(\delta t) = \int_{t_1}^{t_2} S_1(t)S_2(t - \delta t)dt \quad (7)$$

Here, S_1 and S_2 are the time-varying components of each signal. The time shift, Δt , equals the value of the correlation time, δt , that maximizes $C(\delta t)$. The mean axial velocity component, V , is then determined from

$$V = \frac{\Delta l}{\Delta t} = \frac{\Delta l'}{M\Delta t} \quad (8)$$

In these investigations, several shapes of nozzle were examined for their influence on the resulting plasma jet properties. As is common for DC arcjets, the nozzle served also as the anode. Fig. 4 shows the three anode types tested, in cutaway view. We will refer to the nozzle types as A, B, and C, as shown. All nozzles employed tangential inlet passages at their inlet, to stabilize the arc with swirl about the cathode. The standard geometry (type A), which was employed in our first spray studies [10], converged to a short straight nozzle of diameter

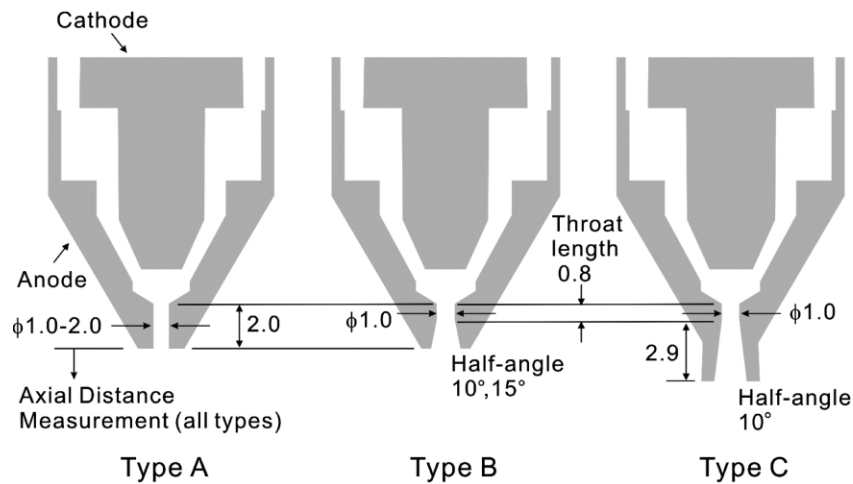


Fig. 4. Cutaway views of the three types of arcjet nozzles investigated. Dimensions in millimeters. Swirl-inducing gas injectors omitted for simplicity.

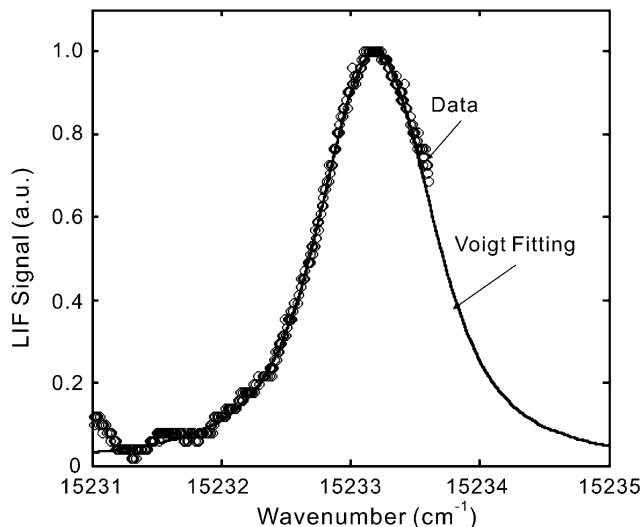


Fig. 5. Typical measured LIF excitation spectrum, taken by varying the laser wavelength across the H_{α} transition, and its Voigt fit. [Type C nozzle, chamber pressure 2.4 kPa, arc power 1.95 kW (30 A \times 65 V), argon flow rate 3.7 sl min^{-1} , hydrogen flow rate 3.0 sl min^{-1} .]

that was varied from 1 to 2 mm. The other two nozzle types had throats of diameter 1 mm, followed by short (type B) or long (type C) conical diverging sections of angles as noted in the figure. Table 1 summarizes the nozzle parameters, as well as the other key operating conditions, for the experiments. Axial positions were measured relative to the exit plane of the short nozzles (types A and C). At any given axial location, the center reference for radial position was taken to be where the absorption due to the H_{α} transition was found to be a maximum.

4. Results and discussion

Fig. 5 shows a typical LIF excitation spectrum, taken by varying the laser wavelength across the H_{α} transition and thus collecting the spectral fluorescence through the bandpass filter. Also shown in the plot is the corresponding Voigt lineshape fit to the spectrum, to extract both the Stark (Lorentzian) and Doppler (Gaussian) components. These data were collected at the exit of a type C nozzle, at a chamber pressure of 2.4 kPa, an arcjet power of 1.95 kW (30 A, 65 V), and argon and hydrogen plasma gas flow rates of 3.7 sl min^{-1} and 3.0 sl min^{-1} , respectively. The Voigt fit, which is found to capture the lineshape reasonably well, yields a temperature of 1800 K and an electron density of approximately $1 \times 10^{20} \text{ m}^{-3}$. The uncertainties in temperature and electron density correlate to the signal-to-noise ratios near the core and in the wings of the lineshape, respectively. This is due to the respective dominance of Doppler and Stark broadening in those spectral regions. For this example, the uncertainties in T and n_e are

estimated to be approximately 17% and 25%, respectively.

Detailed saturation studies were not carried out in this work, since past LIF measurements performed by our group in lower pressure (~ 0.1 kPa) hydrogen arcjet flows [16] indicated that H_{α} lineshapes were not saturated at comparable laser spectral irradiances used in our studies.

The signal-to-noise ratio for LIF varied greatly depending on the discharge conditions. For example, for a chamber pressure of 3.7 kPa, with all other discharge conditions held constant, the LIF spectrum degraded relative to the spectrum for lower pressures. The concomitant increase in noise with chamber pressure was attributed to background plasma emission.

On the other hand, laser absorption measurements were found to have very good signal-to-noise ratios over a broader range of plasma conditions. Therefore, they were used widely, even though jet asymmetry prevented the use of an Abel inversion as mentioned above. Most of the temperature data shown were based instead on an analysis of the direct line-of-sight absorption spectra. Thus, they provide only a qualitative indication of the variation in the jet temperature. The inaccuracy in the line-of-sight data, due to radial variation of temperature and population of the excited absorbing state, is reflected in the discrepancies in Fig. 6. It is assumed, due to the similarity in size and shape of the plume over the conditions studied, that the line-averaged data are nonetheless sufficiently repeatable for use in comparison of varying operating conditions and nozzle configurations.

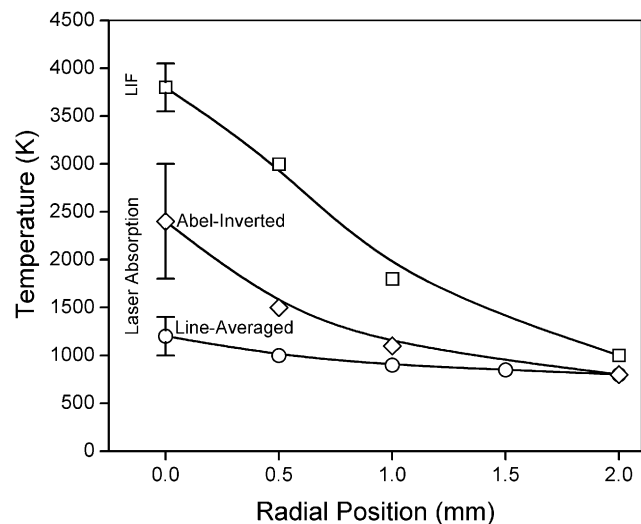


Fig. 6. Comparison of radial temperature profiles measured by three different methods: directly by LIF; by Abel inversion of laser absorption spectra; by direct analysis of laser absorption spectra. [At axial position 4 mm, Type C nozzle, chamber pressure 2.4 kPa, arc power 1.95 kW (30 A \times 65 V), argon flow rate 3.7 sl min^{-1} , hydrogen flow rate 3.0 sl min^{-1} .]

Fig. 6 compares the three types of temperature data. For typical spray conditions, except with pressure decreased to enhance the LIF signal-to-noise, Fig. 6 shows the radial temperature profile in the plasma jet as obtained from LIF and Abel-inverted absorption data. Also shown is the temperature inferred from direct analysis of the line-of-sight absorption spectra (which assumes a uniform plasma along the line-of-sight), and presented for various lateral positions across the jet. The inverted absorption data are found to result in temperatures that appear to be lower than those determined by LIF, although it is noted here that part of this difference can be attributed to the difficulty in reproducing the precise downstream axial locations for the two measurements. It was found that the axial locations can differ by as much as 1 mm, and, over the course of a mm in the axial direction, a change in temperature of approximately 1000 K is not unexpected. Another possible source for the discrepancy is a possible jet asymmetry. Note that the line-of-sight absorption analysis further underestimates temperature, especially through the core region where gradients are highest.

These measurements reveal that although reasonably high temperatures are generated near the exit of the nozzle under conditions typically employed for LPPS, significant radial gradients in temperature (up to 2000 K mm^{-1}) can exist in this low-power arcjet plasma source. Such strong radial energy flows can have a significant consequence on the thermal history of injected particles in plasma spray deposition, since a large fraction of the particles have trajectories that can traverse a large radial distance. These results underscore the importance of precise entrainment of powder in the jet core in this low-power LPPS system, in order to heat the particles sufficiently.

Fig. 7 shows the velocity distribution inferred from the emission correlation measurements, for typical spray conditions. The velocities are plotted vs. the lateral displacement from the centerline. Although the emission was collected with focusing optics, adjusted so that the focal plane was the jet mid-plane, path-averaged out-of-plane emission contributes noise to the signal.

For this measurement, to estimate the depth of field, or the extent of effective measurement volume in the out-of-plane direction, one must consider two effects. First, the focusing optics alone ($F/18$, $M=1.2$, detector diameter = 0.063 mm) produce a depth of field of approximately 1.0 mm. Second, all of the measurements were done in the jet mid-plane, where the temperatures are highest for a given lateral position, so the emittance is at a maximum in the focal plane. The radial eccentricities of up to 0.5 mm for this jet may offset this advantage, yielding an estimated net effective depth of field of 1.0 mm. The spatial resolution in the axial direction is also approximately 1 mm, due to the spacing between the detectors. We obtained strong peaks from

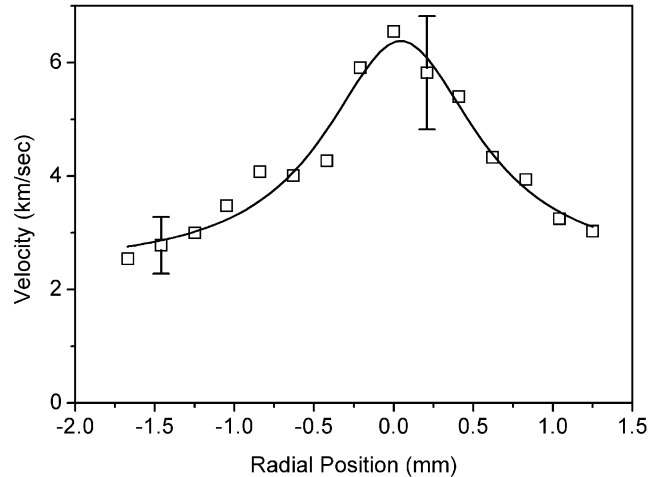


Fig. 7. Velocity profile by emission correlation measurement. Typical spray conditions, axial position 2 mm. Type A nozzle, chamber pressure 5.2 kPa, arc power 1.50 kW ($20 \text{ A} \times 75 \text{ V}$), argon flow rate 3.7 sl min^{-1} , hydrogen flow rate 3.0 sl min^{-1} .

the correlation calculations, indicating that the spatial averaging of out-of-plane velocities due to depth of field was not excessive. The averaging that did occur would have slightly reduced the radial velocity gradients as measured, further emphasizing the conclusion below. The lateral diameter of the detected area is only approximately 0.052 mm , due to the small size of the detectors. The effective measurement volume is approximately 0.002 mm^3 .

The velocity profiles display significant radial asymmetry, similar to that found in the temperature field. It is also clear from Fig. 7, that while very high axial jet velocities (approx. 7 km s^{-1}) are generated near the exit plane of this LPPS source, there is a substantial radial gradient in the axial velocity most likely due to the highly viscous nature of these low-pressure, supersonic flows. Radial gradients of approximately $3 \text{ km s}^{-1} \text{ mm}^{-1}$ are not uncommon. This measurement again reinforces the need for precise powder injection as well as the challenge of achieving it in the presence of such a velocity field.

The choice of nozzle diameter significantly influences the temperature and velocity fields of the plasma jet. In Fig. 8, we illustrate this effect for type A nozzles with diameters in the range of 1.0–1.6 mm. Fig. 8a presents absorption measurements characterizing the radial temperature profile at a fixed downstream axial position of 5 mm. Fig. 8b shows correlation method measurements of axial velocity for positions on the jet centerline. Since they come from line-of-sight data, the temperatures extracted should constitute lower bounds on the actual temperatures in the jet. The plasma conditions for the results shown here are flow rates of 3.7 sl min^{-1} argon, 3.0 sl min^{-1} hydrogen, current of 30 A, and chamber pressure of 5.2 kPa. These conditions are very common

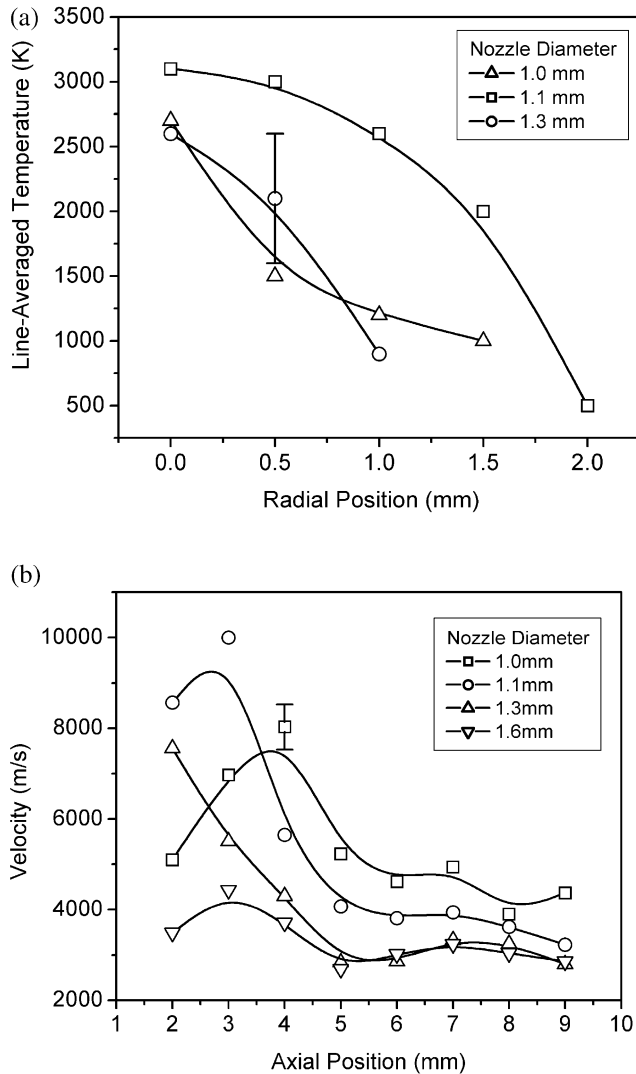


Fig. 8. Effect of nozzle diameter on temperature and velocity. Type A nozzle, chamber pressure 2.7 kPa, arc power 1.95 kW (30 A \times 65 V), argon flow rate 3.7 sl min⁻¹, hydrogen flow rate 3.0 sl min⁻¹. (a) Radial temperature profiles at axial position 5 mm. (b) Axial profiles of axial velocity, measured from emission along chords intersecting the jet axis.

for our LPPS studies. It is seen that higher upstream temperatures and axial velocities are achieved with an intermediate nozzle diameter of 1.1 mm. All else being equal, larger diameter nozzles (e.g. 1.3 mm and 1.6 mm) resulted in generally lower plasma jet temperatures and velocities. For the larger diameters, the arc voltage was also observed to be less stable. These measured and observed effects would be consistent with reduced thermal efficiency of the torch for the larger diameters, though detailed efficiency measurements were not carried out for these cases. For these gas mixtures, this plasma torch has thermal efficiency defined as net power to plume divided by arc input power, of 50%–65%.

The axial velocity data also clearly identify the presence of recurring diamond shocks, the first and strongest of which occurs closer to the exit of the nozzle for the smaller nozzle diameters. The diamond shock pattern is often visible as thin, dark, oblique lines in the glowing plume.

A comparison is made of velocity profiles for the three nozzle types in Fig. 9. All three nozzles had a 1.1 mm diameter for their straight sections. The plasma conditions for the results shown here are flow rates of 3.7 sl min⁻¹ argon, 3.0 sl min⁻¹ hydrogen, a current of 30 A, and a chamber pressure of 5.3 kPa. The nozzles with 10° diverging sections produced higher velocities overall, with maximum velocities in excess of 5 km s⁻¹. Furthermore, use of the longer (type C) 10° nozzle resulted in overall higher velocities at positions further from the nozzle exit.

As expected, increasing the arc power dramatically increases both temperature and velocity in the plasma jet. Fig. 10a shows temperatures measured at an axial position of 5 mm, for discharge conditions similar to those of Fig. 9 but varying arc current. The analogous velocity measurements, of Fig. 10b, were taken at a reduced hydrogen flow rate (1.5 sl min⁻¹) and at reduced chamber pressure (1.1 kPa). In general, it is observed that gas-dynamic shock features become more pronounced at the higher discharge powers. These are also the conditions of maximum Mach number, calculated to be approximately Mach 5 for 8 km s⁻¹ at 4000 K with incomplete hydrogen dissociation. The successive shock waves seen to be prominent at the higher powers eventually dissipate kinetic energy and result in a downstream velocity that is comparable to that of the lower discharge power. For spraying purposes, the ben-

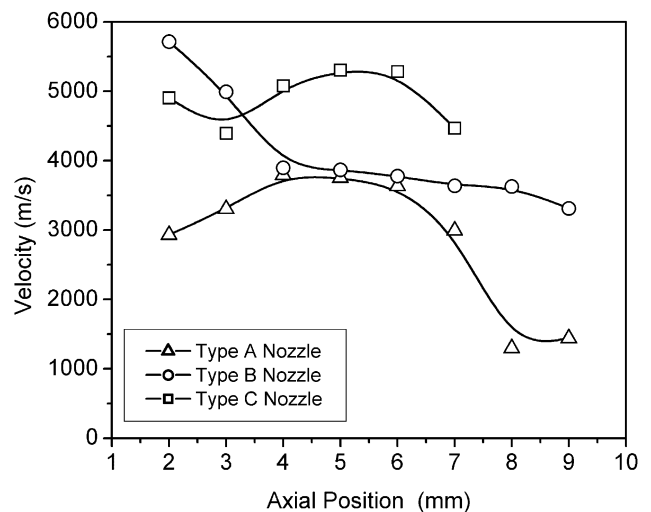


Fig. 9. Comparison of axial profiles of axial velocity for the three nozzle geometries. Chamber pressure 5.3 kPa, arc power 1.95 kW (30 A \times 65 V), argon flow rate 3.7 sl min⁻¹, hydrogen flow rate 3.0 sl min⁻¹.

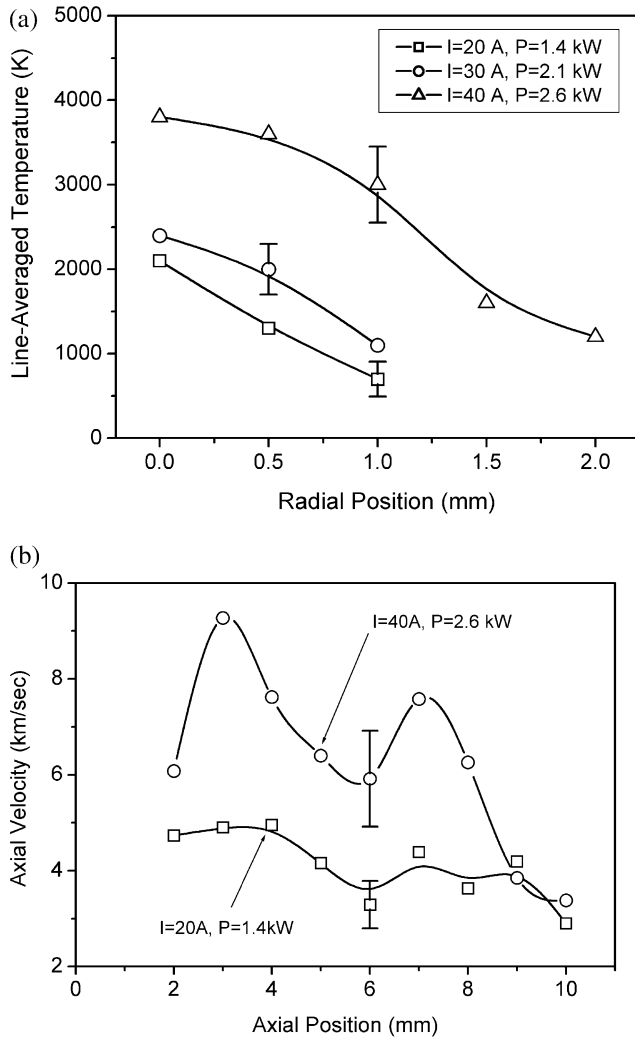


Fig. 10. Effect of plasma arc power on temperature and velocity. (a) Radial temperature profiles at axial position 5 mm. Type C nozzle, chamber pressure 5.2 kPa, argon flow rate 3.7 sl min⁻¹, hydrogen flow rate 3.0 sl min⁻¹. (b) Axial profiles of axial velocity, measured from emission along chords intersecting the jet axis. Type A nozzle of diameter 1.1 mm, chamber pressure 1.1 kPa, argon flow rate 3.7 sl min⁻¹, hydrogen flow rate 1.5 sl min⁻¹.

efit of higher arc power is not lost due to shocks, since the decreased kinetic energy is recovered as enthalpy.

The addition of hydrogen to the flow, while increasing the enthalpy due to increased arc voltage, is found to have an unexpected impact on the temperature of the plasma jet. Fig. 11 shows the effect of increased hydrogen flow on the temperature profile measured at an axial location of $z=5$ mm and at a chamber pressure of 5.2 kPa. Plasma temperature was maximized, at this axial location, by an intermediate hydrogen flow rate of 2 sl min⁻¹. Above 2 sl min⁻¹, the benefit of increased discharge power was apparently offset by the increased heat capacity due to addition of a diatomic gas. The molar specific heat of the Ar/H₂ mixture increases with H₂ fraction, not to mention the energy absorbed through

dissociation of hydrogen. Some of this temperature deficit may be recovered in plasma–particle heat transfer through the corresponding gains in plasma thermal conductivity. Thermal conductivity of a non-reacting gas mixture is proportional to its specific heat, and dissociated H₂ further increases the effective thermal conductivity through recombination on the particle.

A series of measurements of the local translation temperature (as determined by LIF), electronic excitation temperature (by the ratio of intensities of the H_β and H_α spectral lines), and of the local electron density (from the Lorentzian component of the LIF spectral line) were performed at a fixed axial location ($z=5$ mm and $r=0$ mm) and varying chamber pressures. The results are displayed in Fig. 12 for the type C nozzle. The higher chamber pressure reduces the tendency for the jet to expand, and, as expected, results in a higher electron density. We find that there is a nearly linear relation between the electron density and chamber pressure, as seen in Fig. 12b. On the other hand, at the higher pressure, the gas temperature is seen to decrease—a result attributed to the entrainment of colder chamber gas near the plasma jet boundary. While the gas temperature decreases due to this entrainment, the excitation temperature, which is elevated well above that of the gas temperature (due to an elevated electron temperature) is seen not to vary substantially. This later result is not unexpected, as the electron energy relaxation is slow, due to the disparity between the electron and atomic hydrogen mass.

The effects of varying chamber pressure on the axial velocity are displayed in Fig. 13, for experiments performed with the short, 10° divergent nozzle. It is expected that variations in the chamber pressure will affect both the location and strength of the shock

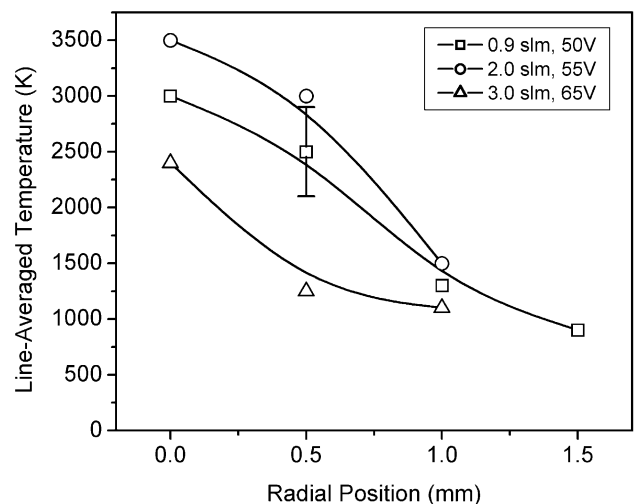


Fig. 11. Effect of hydrogen flow rate on temperature at axial position 5 mm. Type C nozzle of diameter 1.1 mm, chamber pressure 5.2 kPa, arc current 30 A, argon flow rate 3.7 sl min⁻¹.

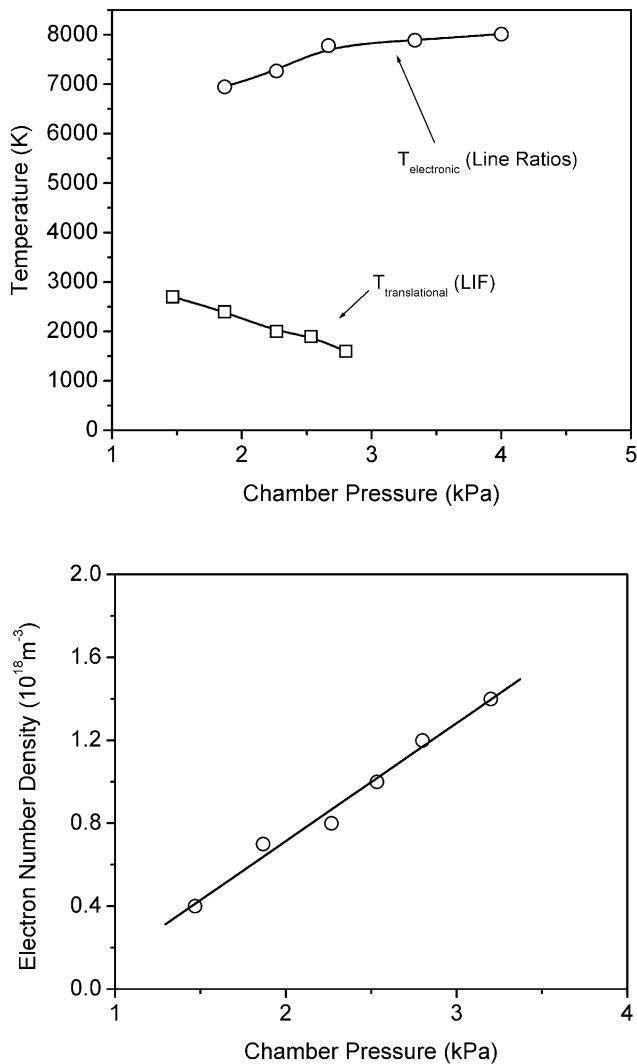


Fig. 12. Effect of chamber pressure on temperature and electron density. Type C nozzle of diameter 1.1 mm, arc power 1.50 kW (30 A \times 75 V), argon flow rate 3.7 sl min^{-1} , hydrogen flow rate 3.0 sl min^{-1} . (a) Translational temperature and electronic temperature. (b) Electron density.

features, as seen from the measured axial variation in the velocity for a relatively low pressure (1.1 kPa) and high-pressure (7.3 kPa) condition shown in Fig. 13a. The plasma conditions for the results shown here are gas flow rates of 3.7 sl min^{-1} of argon, 1.0 sl min^{-1} of hydrogen, a current of 20 A, and a voltage of 75 V. The location of diamond shocks will move upstream with increased chamber pressure, as the expansion waves are reflecting off a jet boundary that is reduced in diameter. Measurements taken at a fixed axial location ($z=4$ mm) in the long, 10° divergent nozzle, with varying pressure (Fig. 13b) shows a strong maximum most likely the result of the upstream passage of a strong shock across the measurement volume as the pressure is increased. The maximum velocity, which is seen at a pressure of approximately 4.0 kPa for the long

nozzle, is approximately 7 km s^{-1} . In this figure, gas flow rates of 3.7 sl min^{-1} of argon, 3.0 sl min^{-1} of hydrogen, a current of 30 A, and a voltage of 75 V.

Fig. 14 shows the effect of carrier gas flow rate on the atomic hydrogen temperature distribution, measured by the inverted laser absorption method. The radial temperature gradient was estimated to be 200–2000 K mm^{-1} and the gradient near center of the plasma, $r < 1$ mm, was 1/10 to 1/3 lower than that at far from the center, $r > 1$ mm. It was also found that temperature increased with carrier gas flow rate in this study range. As mentioned above, argon atoms may increase the rate of hydrogen recombination reaction that releases heat in the form of thermal energy.

5. Summary and conclusions

The temperature measurements were carried out using laser absorption and LIF techniques based on a Voigt

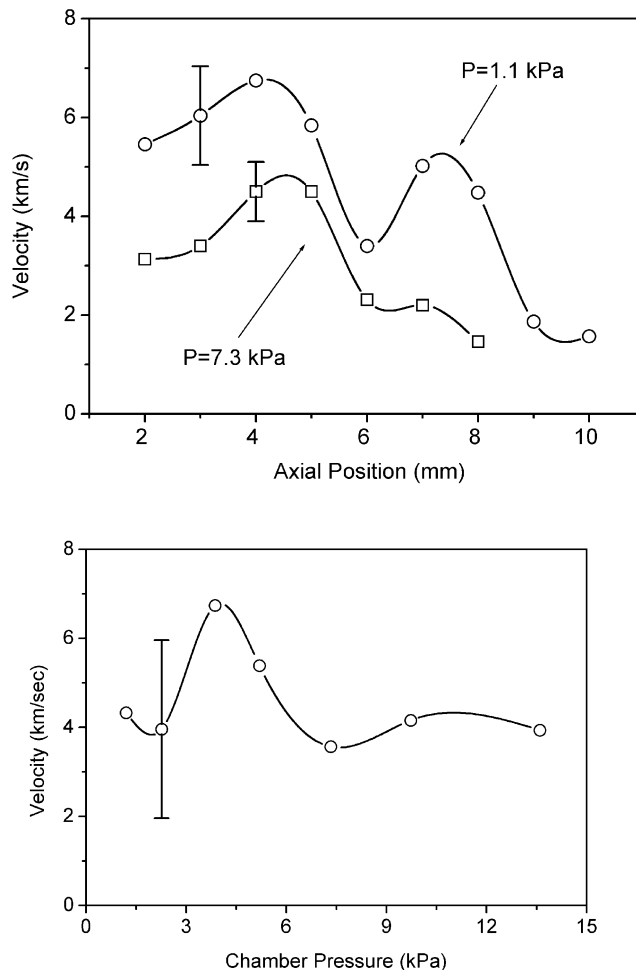


Fig. 13. Effect of chamber pressure on axial velocity. (a) Axial profiles of velocity at 1.1 kPa and 7.3 kPa. Type B nozzle of diameter 1.1 mm, arc power 1.50 kW (20 A \times 75 V), argon flow rate 3.7 sl min^{-1} , hydrogen flow rate 1.0 sl min^{-1} . (b) Axial velocity vs. chamber pressure at axial position 4 mm. Type C nozzle of diameter 1.1 mm, arc power 2.15 kW (30 A \times 75 V), argon flow rate 3.7 sl min^{-1} , hydrogen flow rate 3.0 sl min^{-1} .

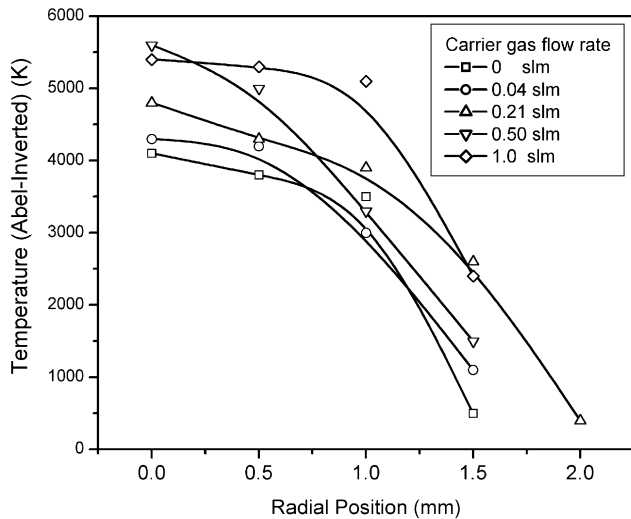


Fig. 14. Effect of carrier gas flow rate on temperature at axial position 5 mm. Type A nozzle of diameter 1.1 mm, chamber pressure 5.2 kPa, arc power 1.95 kW (30 A \times 65 V), argon flow rate 3.7 sl min⁻¹, hydrogen flow rate 3.0 sl min⁻¹.

fit of the lineshapes of the Balmer- α transition. Even though the accuracy was lower than the other methods, because it was easier to implement and signals were less noisy, laser absorption without inversion was mainly used to evaluate the effect of the plasma gun shape and plasma conditions on the temperature distribution. Also, laser absorption with inversion and LIF were performed to obtain more accurate temperature measurements in cases where it was possible to obtain good signals.

In light of the advantages of LIF temperature measurements for spatial resolution and hence for overall accuracy in an asymmetric temperature field such as this one, it should be noted that the LIF system could be improved to extend its usability to higher pressures. The signal-to-noise ratio for LIF at higher pressures would be improved by simply replacing the excitation laser with one of greater instantaneous power. A pulsed laser, with gated data acquisition, is often used for achieving high instantaneous power. The benefit of increased laser power is limited by the saturation intensity of the LIF transition for the plasma conditions of interest. A calculation of saturation intensity [16] must therefore be made before specifying the laser for an LIF system.

The measured temperature and velocity were strongly dependent on the plasma nozzle shape. It was found that a relatively long throat and 10° divergent nozzle resulted in a higher maximum velocity and a lower velocity gradient in the axial (jet) direction. The maximum velocity and the velocity gradient in the axial direction were measured to be more than 7 km s⁻¹ and 1 km s⁻¹ mm⁻¹, respectively. For thermal spraying purposes, ease of particle entrainment and uniformity of

particle transport and heating are enhanced by broadening the jet's momentum core and reducing the radial and axial gradients in velocity. These considerations are especially critical in this small-scale spray system. Similarly critical is the breadth of the jet's thermal core, and the minimization of radial and axial temperature gradients. From the standpoints of momentum and heat transfer to particles, it was determined that a nozzle with a relatively long diverging section (type C) was the best geometry for low-power LPPS.

It was also found that the input power, chamber pressure, hydrogen flow rate, and carrier gas flow rate affected the plasma temperature and velocity. As expected, the measured temperature increased with increasing arc power (ranging between 1 and 3 kW). Several other effects were observed that were less predictable. The plasma temperature was maximized, in the range 4.0–9.3 kPa, approximately 5.3 kPa. The plasma temperature was also maximized at hydrogen flow rates approximately 2 sl min⁻¹, due possibly to a balance between temperature rise and dissociation fraction. Finally, the introduction of up to 1 sl min⁻¹ carrier gas flow was observed surprisingly to cause an increase in measured temperatures, possibly by promoting the recombination of hydrogen ions with electrons. These surprising results warrant further study if they are deemed to impact substantially the conditions for plasma spraying.

References

- [1] L. Pawlowski, *The Science and Engineering of Thermal Spray Coatings*, John Wiley & Sons, Chichester, UK, 1995.
- [2] C. Moreau, L. Leblanc, *Key Eng. Mater.* 197 (2001) 22.
- [3] H. Hamatani, N. Shimoda, Y. Ichiyama, S. Kitaguchi, T. Saito, *Funct. Gradient Mater.* 34 (1992) 385.
- [4] H.D. Steffens, *Proceeding of the 7th International Conference on Vacuum Metallurgy*, Tokyo, 1982, p. 295.
- [5] P. Chraska, J. Dubsy, K. Neufuss, J. Pisacka, *JTST* 6 (3) (1997) 325.
- [6] M. Vardelle, A. Vardelle, A.C. Leger, P. Fauchais, D. Gobin, *JTST* 4 (1) (1995) 50.
- [7] T. Zhang, D.T. Gawne, B. Liu, *Surf. Coat. Technol.* 132 (2000) 233.
- [8] R. Merz, F. Prinz, K. Ramaswami, K. Terk, L. Weiss, *Shape deposition manufacturing*, *Proceedings of the Solid Freeform Fabrication Symposium*, University of Texas at Austin, Austin, Texas, 1994, p. 1.
- [9] A.G. Cooper, S. Kang, J. Stampfl, F.B. Prinz, *Fabrication of ceramic parts for a miniature jet engine application using Mold SDM*, in: J.P. Singh, N.P. Bansal, K. Nihara (Eds.), *Innovative Processing and Synthesis of Ceramics, Glasses and Composites III*, *Ceram. Trans.* 108 (2000) 389.
- [10] W.S. Crawford, H. Hamatani, M.A. Cappelli, F.B. Prinz, *International Conference on Plasma Science*, 1999, p. 194.
- [11] J.G. Liebeskind, Ph.D. Thesis, Stanford University, Stanford, California, 1994.
- [12] H.R. Griem, *Contrib. Plasma Phys.* 40 (1–2) (2000) 46.
- [13] H.R. Griem, *Plasma Spectroscopy*, McGraw-Hill, New York, 1964.
- [14] D.E. Kelleher, W.L. Wiese, V. Helbig, R.L. Greene, D.H. Oza, *Phys. Scr.* T47 (1993) 75.

- [15] P.V. Storm, M.A. Cappelli, *Appl. Opt.* 35 (1996) 4913.
- [16] P.V. Storm, Ph.D. Thesis, Stanford University, Stanford, California, 1997.
- [17] C. Stehle, N. Feautier, *J. Phys. B: At. Mol. Phys.* 17 (1984) 1477.
- [18] B. Glocker, M. Auweter-Kurtz, *AIAA Paper* 92-3835, July 1992.
- [19] W. Juchmann, J. Luque, J.B. Jeffries, *Appl. Opt.* 39 (21) (2000) 3704.
- [20] P. Fauchais, A. Vardelle, A. Denoirjean, *Surf. Coat. Technol.* 97 (1997) 66–78.
- [21] J.A. Pobst, R.A. Spores, J.H. Schilling, D.A. Erwin, *J. Propul. Power* 12 (6) (1996) 1107.
- [22] A.H. Shapiro, *The Dynamics and Thermodynamics of Compressible Fluid Flow*, vol. I, The Ronald Press Company, 1953.
- [23] M. Mitcher, C.H. Kruger, *Partially Ionized Gases*, John Wiley & Sons, New York, 1992.
- [24] W.C. Kreye, J.W. Hemsley, M.J. Andrews, *J. Phys. D: Appl. Phys.* 26 (1993) 1836.